PCCP

Accepted Manuscript

ROYAL SOCIETY OF CHEMISTRY

www.rsc.org/pccp

Journal Name

ARTICLE TYPE

Cite this: DOI: 10.1039/xxxxxxxxxx

Coupled phase field, heat conduction, and elastodynamic simulations of kinetic superheating and nanoscale melting of aluminum nanolayer irradiated by picosecond laser

Yong Seok Hwang[a] and Valery I. Levitas[b]

Received Date
Accepted Date

DOI: 10.1039/xxxxxxxxxx

www.rsc.org/journalname

An advanced continuum model for nanoscale melting and kinetic superheating of an aluminum nanolayer irradiated by a picosecond laser is formulated. Barrierless nucleation of surface premelting and melting occurs, followed by a propagation of two solid-melt interfaces toward each other and their collision. For a slow heating rate of $Q = 0.015\,K/ps$ melting occurs at the equilibrium melting temperature under uniaxial strain conditions $T^{\epsilon}_{eq} = 898.1K$ (i.e., below equilibrium melting temperature $T_{eq} = 933.67\,K$) and corresponding biaxial stresses, which relax during melting. For a high heating rate of $Q = 0.99 - 84\,K/ps$, melting occurs significantly above T_{eq}. Surprisingly, an increase in heating rate leads to temperature reduction at the 3 nm wide moving interfaces due to fast absorption of the heat of fusion. A significant, rapid temperature drop ($100 - 500K$, even below melting temperature) at the very end of melting is revealed, which is caused by the collision of two finite-width interfaces and accelerated melting in about the 5 nm zone. For $Q = 25 - 84\,K/ps$, standing elastic stress waves are observed in a solid with nodal points at the moving solid-melt interfaces, which, however, do not have a profound effect on melting time or temperatures. When surface melting is suppressed, barrierless bulk melting occurs in the entire sample, and elastodynamic effects are more important. Good correspondence with published, experimentally-determined melting time is found for a broad range of heating rates. Similar approaches can be applied to study various phase transformations in different materials and nanostructures under high heating rates.

Melting of metals induced by ultra-fast laser heating has been studied for the past several decades from both academic and applied points of view. **In industrial applications, ultra-fast heating and melting of metals are utilized for various purposes, even without a full understanding of melting mechanisms. Examples include the reforming of micron particles (and hence producing nanoparticles [1]), production of hollow nanoparticles [2], laser-induced forward transfer (LIFT) [3], light-induced rapid annealing (LIRA) [4] and nano-structuring [5].** Ultra-fast heating and melting are parts of more complex phenomena like fast combustion of metallic nanoparticles [6] and LIFT of a nanolayer [3]. From basic perspectives, many theoretical, computational, and experimental studies have been dedicated to this topic (see reviews [6–8]); however, there are still remaining puzzles, especially for extreme conditions, which enable kinetic superheating. A melting mechanism under such high heating rates is not governed by thermodynamics only but rather by a combination of thermodynamics, kinetics, thermal conduction, mechanics, and several nanoscale effects, as well as their coupling. **As will be shown, nanoscale effects are related to several characteristic dimensions. Two of them are the width of a sample ($w = 25\,nm$) and variable distance between moving interfaces where a standing elastic wave is localized, which also depends on w. Three other scale parameters are independent of w: (a) width of a pre-molten surface layer ($1\,nm$) where melt nucleates; (b) width of a propagating solid-melt interface ($3\,nm$) within which all transformation-related processes occur, and (c) size of interface collapse region ($5\,nm$) where temperature drops drastically.** Simple models [9–12], which assumed that homogeneous melt nucleation is the only mechanism, have failed to reproduce the superheating temperature observed in the experiments [13–15]. It is known that fast heating can produce elastic waves [16] and these waves can interact with thermal physics by thermoelastic coupling. In the same way, phase transformation is coupled to thermal conduction, in particular through latent heat and the effect of temperature on the kinetics of melting. Recent experimental study for a TiNi shape memory alloy also reported the observation of nanoscale temperature variation coupled with mechanical loading and phase **transformation [17]. Note** that properties of the shape memory alloys are highly sensitive to the temperature [17]. Coupled models for the melting of

[a] *Department of Aerospace Engineering, Iowa State University, Ames, Iowa 50011, U.S.A. E-mail: yshwang@iastate.edu*

[b] *Departments of Aerospace Engineering, Mechanical Engineering, and Material Science and Engineering, Iowa State University, Ames, Iowa 50011, U.S.A. Fax: +1 801 788 0026; Tel: +1 515 294 9691; E-mail: vlevitas@iastate.edu*

metals, irradiated by an ultrafast laser, that include mechanics and the two temperature model (TTM) for heating have been suggested **in Ref.[16,18]. However,** they did not include kinetics of melting and were not able to resolve superheating or the coupling of phase transformation with temperature evolution. The melting models coupled to TTM for heating and an interface-tracking model based on melt nucleation kinetics were developed **in Ref.[19,20]. However,** they did not include mechanics and coupling between temperature evolution and mechanics. The model in Ref.[21] was focused on heating processes without the kinetics of melting and elastic waves.

Recently[15], we have suggested a phase field approach, which combined melting with the TTM for heating and mechanics. It was successfully applied to the study of kinetic superheating and melting beyond the theoretically-predicted ultimate superheating limit of aluminum, for example, $1.38\,T_{eq}$, based on the entropy catastrophe[22]. However, this model has several drawbacks: temperature evolution includes laser heating only and neglects coupling to melting (latent heat of fusion) and **mechanics. Also,** the static equilibrium equation was used instead of the dynamic equation of motion. This could result in an overestimation of kinetic superheating temperature and inaccuracy in melting kinetics. In Ref.[23], this model was expanded by developing a new lattice temperature evolution equation, which takes into account thermoelastic coupling, transformation heat, and the dissipation rate due to phase transformation. It was applied to a relatively slow heating rate; it was demonstrated that internal stresses can reduce the melting temperature for an Al nanolayer below the bulk melting temperature, T_{eq}. Still, mechanical equilibrium was imposed and electron temperature and electron-phonon coupling were neglected. In the current research, in order to study higher heating rates, we further improved our model. Thus, we included advanced thermomechanical coupling, transformation heat, and the dissipation rate due to melting in the TTM and substituted the elastostatic formulation with an elastodynamic one. The melting of a free standing aluminum nanolayer irradiated by a picosecond laser[14] is simulated and compared with experimentally observed melting times to verify the validity of the model, and with the results of a simplified model[15]. The details of melting and superheating physics are analyzed and some surprising effects have been revealed. In particular, an increase in heating rate leads to temperature reduction at the moving solid-melt interfaces due to fast absorption of the latent heat. Also, a sharp temperature decrease exceeding several hundred K (even below melting temperature) at the final stage of melting occurs, which is caused by a collision of two interfaces and accelerated melting. When surface melting is suppressed, barrierless bulk melting occurs in the entire sample above the instability temperature of the solid, promoted by elastodynamic effects.

1 Phase field, temperature evolution, and elastodynamic models

Governing equations are comprised of the coupled Ginzburg-Landau equation for melting, equations of elastodynamics or elastostatics, and the TTM which includes contributions due to heat of fusion, thermoelastic effects, and dissipation due to melting. They represent further development of equations formulated in Ref.[15,23–25].

Kinematics. Total strain tensor $\boldsymbol{\varepsilon} = (\boldsymbol{\nabla}_0 \boldsymbol{u})_s$ is decomposed into elastic $\boldsymbol{\varepsilon}_e$, transformation $\boldsymbol{\varepsilon}_t$, and thermal $\boldsymbol{\varepsilon}_\theta$ strains in an additive way:

$$\boldsymbol{\varepsilon} = \boldsymbol{\varepsilon}_e + \boldsymbol{\varepsilon}_t + \boldsymbol{\varepsilon}_\theta; \;\; \boldsymbol{\varepsilon} = 1/3\varepsilon_0 \boldsymbol{I} + \boldsymbol{e}; \tag{1}$$

$$\boldsymbol{\varepsilon}_{in} = \varepsilon_{in}\boldsymbol{I} = \boldsymbol{\varepsilon}_t + \boldsymbol{\varepsilon}_\theta; \;\; \boldsymbol{\varepsilon}_t = 1/3\varepsilon_{0t}\,(1-\phi\,(\eta))\,\boldsymbol{I}; \tag{2}$$

$$\boldsymbol{\varepsilon}_\theta = \alpha_s \left(T_{eq} - T_0\right)\boldsymbol{I} + (\alpha_m + \Delta\alpha\phi\,(\eta))\left(T - T_{eq}\right)\boldsymbol{I}. \tag{3}$$

Here, $\boldsymbol{u}$ is the displacement vector; $\boldsymbol{\nabla}_0$ is the gradient operator in the undeformed state; the subscript s designates symmetrization; η is the order parameter ($\eta = 1$ represents solid and $\eta = 0$ is melt), α_s and α_m are the linear thermal expansion coefficients for solid and melt, respectively; $\Delta\alpha = \alpha_s - \alpha_m$, $\boldsymbol{I}$ is the unit tensor; T_0 is the reference temperature; ε_0 is the total volumetric strain; ε_{0t} is the volumetric transformation strain for complete melting; $\boldsymbol{e}$ is the deviatoric strain, and $\phi\,(\eta) = \eta^2\,(3-2\eta)$ is the interpolation function for variation of any material property between solid and melt.

Free energy. Free energy per unit undeformed volume is formulated as in Ref.[15,24]:

$$\psi = \psi^e + J\breve{\psi}^\theta + \psi^\theta + J\psi^\nabla; \;\; \breve{\psi}^\theta = A\eta^2(1-\eta)^2; \tag{4}$$

$$\psi^e = 0.5K\varepsilon_{0e}^2 + \mu \boldsymbol{e}_e : \boldsymbol{e}_e; \;\; \psi^\theta = H(T/T_{eq} - 1)\phi(\eta); \tag{5}$$

$$\psi^\nabla = 0.5\beta|\boldsymbol{\nabla}\eta|^2, \;\; A := 3H(1 - T_c/T_{eq}), \tag{6}$$

where $\breve{\psi}^\theta$, ψ^e, ψ^θ, and ψ^∇ are the double-well, elastic, thermal, and gradient energy, respectively; ρ_0 and ρ are the mass densities in the undeformed and deformed states, respectively; $J = \rho_0/\rho = 1 + \varepsilon_0$; $K(\eta) = K_m + \Delta K\phi(\eta)$ and $\mu(\eta) = \mu_s\phi(\eta)$ are the bulk and shear moduli, where $\Delta K = K_s - K_m$; β is the gradient energy coefficient; H is latent heat of fusion; $\boldsymbol{\nabla}$ is the gradient operator in the deformed state; and T_c is the melt instability temperature.

Stresses. A thermodynamic procedure similar to that in Ref.[26–28] leads to the following equations for the stress tensor $\boldsymbol{\sigma}$

$$\boldsymbol{\sigma} = \frac{\partial\psi}{\partial\boldsymbol{\varepsilon}} - J^{-1}\boldsymbol{\nabla}\eta \otimes \frac{\partial\psi}{\partial\boldsymbol{\nabla}\eta} = \boldsymbol{\sigma}_e + \boldsymbol{\sigma}_{st}; \tag{7}$$

$$\boldsymbol{\sigma}_e = K\varepsilon_{0e}\boldsymbol{I} + 2\mu\boldsymbol{e}_e; \;\; \boldsymbol{\sigma}_{st} = (\psi^\nabla + \breve{\psi}^\theta)\boldsymbol{I} - \beta\boldsymbol{\nabla}\eta \otimes \boldsymbol{\nabla}\eta,$$

where $\boldsymbol{\sigma}_e$ and $\boldsymbol{\sigma}_{st}$ are the elastic stresses and interface stresses (interface tension), and $\otimes$ means the dyadic product of vectors. Correct expression for the interface stresses are obtained by using the gradient operator in the deformed state of the gradient energy ψ^∇ and by multiplying $\breve{\psi}^\theta$ and ψ^∇ by the Jacobian J.

Ginzburg-Landau equation. The explicit expression for the thermodynamic driving force X, work-conjugated to the $\dot{\eta}$, can be obtained using the same thermodynamic procedure. A linear relationship between X and $\dot{\eta}$ results in the Ginzburg-Landau equa-

tion for melting:

$$\frac{1}{L}\frac{\partial \eta}{\partial t} = X = -J^{-1}\frac{\partial \psi}{\partial \eta}\Big|_{\boldsymbol{\varepsilon}} + \boldsymbol{\nabla}\cdot\left(J^{-1}\frac{\partial \psi}{\partial \boldsymbol{\nabla}\eta}\right)$$

$$= J^{-1}\{-\varepsilon_{0t}p_e + 3p_e\Delta\alpha(T-T_{eq})\}\frac{\partial \phi}{\partial \eta}$$

$$- J^{-1}\{0.5\Delta K\varepsilon_{0e}^2 + \mu \boldsymbol{e}_e : \boldsymbol{e}_e + H\left(\frac{T}{T_{eq}} - 1\right)\}\frac{\partial \phi}{\partial \eta}$$

$$- 4A\eta(1-\eta)(0.5-\eta) + \beta\nabla^2\eta - \frac{\varsigma}{L}, \qquad (8)$$

where L is the kinetic coefficient, $p_e = \boldsymbol{\sigma}_e : \boldsymbol{I}/3 = -\bar{p}$ is the mean elastic stress, $\bar{p}$ is the elastic pressure **(as usual, compressive pressure is positive)**, and ς is the term that mimics thermal fluctuations.

The equation of motion is written in a traditional form

$$\rho\frac{\partial^2 \boldsymbol{u}}{\partial t^2} = \boldsymbol{\nabla}\cdot\boldsymbol{\sigma}. \qquad (9)$$

It allows the description of elastic waves caused by fast heating and melting. When melting occurs at a time scale much larger than that for an elastic wave, the static equilibrium equation, $\boldsymbol{\nabla}\cdot\boldsymbol{\sigma} = 0$, is used instead.

Two-temperature model. The TTM states that energy absorbed by electron gas near the metal surface spreads over the electron gas by collisions of electrons within the femtosecond time scale and later transfers to a phonon by electron-phonon coupling[29]. The heat transfer mechanism can be represented by the lattice conduction equation, the electron conduction equation, and their coupling:

$$C_l\frac{\partial T}{\partial t} = \boldsymbol{\nabla}\cdot(\kappa_l\boldsymbol{\nabla}T) + G(T_e - T) - 3T(\alpha_m + \Delta\alpha\phi)\frac{\partial p_e}{\partial t}$$

$$+\left(\frac{\partial \eta}{\partial t}\right)^2/L - \left[3p_e\Delta\alpha - \frac{H}{T_{eq}}\right]T\frac{\partial \phi}{\partial \eta}\frac{\partial \eta}{\partial t}, \qquad (10)$$

$$C_e\frac{\partial T_e}{\partial t} = \boldsymbol{\nabla}\cdot(\kappa_e\boldsymbol{\nabla}T_e) + I - G(T_e - T), \qquad (11)$$

where T and T_e are the temperature of lattice and electron gas, respectively, κ_l and κ_e are the lattice and electron thermal conductivity coefficients, respectively, I is the laser power absorbed by the electrons, G is the electron-phonon coupling coefficient, and $C_l = C_{lm} + (C_{ls} - C_{lm})\,\phi(\eta)$ is the lattice heat capacity where C_{lm} and C_{ls} are the heat capacities for melt and solid, respectively. In the lattice heating equation (10), the second term is due to electron-phonon coupling, the third term appears due to thermoelastic coupling, the fourth term is the dissipation due to melting, and the final term is a contribution due to heat of fusion and change in the thermal expansion coefficient during melting. Usually, only heat of fusion is included in the temperature evolution equation[30]. Also, since entropy of fusion H/T_{eq} is considered to be constant, heat of fusion decreases for melting below T_{eq} at slow heating and increases for the high heating rates with overheating.

2 Problem formulation for the laser heating

Experimental observation of the melting of a free-standing aluminum nanolayer with the thickness $w = 25nm$, irradiated by a picosecond laser[14], is simulated. Because the radius of the irradiated spot was much larger than w (mm vs. ns) the problem could be safely considered to be a 1-D problem with zero displacements orthogonal to the laser axis; all parameters vary along the laser axis x only. Figure 1 shows the schematic of a computational domain.

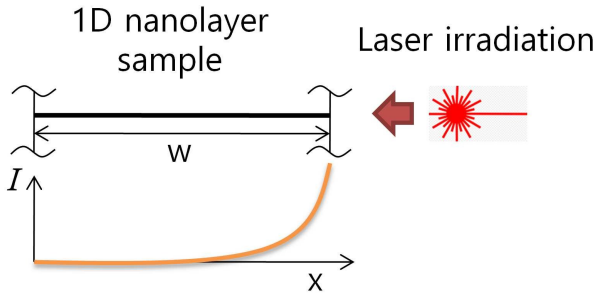

Fig. 1 Schematics of a sample and distribution of irradiated energy.

Six different laser fluences (7, 8, 9, 10, 11, 13 mJ/cm^2) are used in simulations with corresponding pulse durations (1000, 350, 180, 115, 60, 20 ps) in accordance with experimental data[14]. **While the laser beam may have Gaussian fluence distribution orthogonal to the axis across its 4 mm diameter, we operate with averaged fluences due to two reasons. First, in Ref.[14] the averaged laser fluences were measured and reported for the central spot masked by 1 mm diameter hole, and the diameter of examining electron beam was even smaller, namely 500 μm, where the energy distribution on a Gaussian profile is possibly flat. Second, accounting for such a distribution would require consideration of axisymmetric problem with the sample diameter of more than 2 mm, while resolving numerically 1 nm wide surface melt. This is not only computationally prohibitive but also not smart.** Cases with fluences 11 and 13 mJ/cm^2 only are treated in elastodynamic formulation since the time scale for heating for other cases is at least more than an order of magnitude larger than the acoustic time $t_a = \frac{w}{2c} \simeq 3ps$ (i.e., the time of propagation of an elastic wave with velocity $c = 4000\,m/s$ through half of a sample width $w/2$). The finite-element code *COMSOL Multiphysics* was used for the simulations[31].

Boundary and initial conditions, and source terms. Both plane boundaries are stress-free in the case of an elastodynamic problem, and one of the boundaries is fixed to prevent translation and rotation of a sample for elastostatic formulation. Since energy irradiated by the laser is included as a volumetric heat source according to Beer-Lambert law in Eq.(12), the heat flux was zero at both plane boundaries. Attenuation of the laser irradiated is modeled as[16]

$$I = I_0 exp(-\zeta(w-x)); \quad I_0 = \zeta W/(1 - exp(-\zeta w));$$

$$W = (1-R)F_0/t_p, \qquad (12)$$

where ζ is the absorption coefficient, which is $1.21 \times 10^8\, m^{-1}$ for the 1064-nm laser used in the experiment; R is the reflectance, which was accepted as 0 since fully absorbed fluence was reported in experiment[14]; t_p is the pulse duration; and F_0 is the fluence of a laser.

The boundary condition for the order parameter η at the surface with the unit normal $\boldsymbol{n}$ is

$$J\frac{\partial\psi}{\partial\nabla\eta}\cdot\boldsymbol{n} = \beta\nabla\eta\cdot\boldsymbol{n} = -\frac{d\gamma}{d\eta}, \tag{13}$$

where $\gamma(\eta) = \gamma_m + (\gamma_s - \gamma_m)\phi(\eta)$; γ_s and γ_m are the solid-vapor and melt-vapor surface energies, which depend on crystal faces at the surface, the state of the surface, and the surroundings. **Reduction of the surface energy during melting produces an additional driving force for melting, which can lead to barrierless surface premelting (incomplete melt, $\eta > 0$) and melting below the bulk melting temperature. This phenomenon is observed in experiments (see review[7]) and can be described well by boundary conditions Eq.**(13) **(see Ref.[15,23–25].)**

Two regimes will be considered:

(a) The γ_s and γ_m presented in Table 1[23] lead to the surface-induced melt nucleation and correspond to experimental conditions in Ref.[14]. Since for a homogeneous solid phase $\eta = 1$, the driving force $X = 0$ in the Ginzburg-Landau Eq.(8) and $d\gamma/d\eta = 0$ in Eq.(13), one needs some perturbations at the boundary to initiate melting. We use the condition that if at the boundaries $\eta > 1 - \hat{\eta}$, then $\eta = 1 - \hat{\eta}$, where perturbation $\hat{\eta} = 10^{-5}$. Without this condition, even if the initial value of $\eta < 1$, it can return to $\eta = 1$ during heating below the melting temperature and melting could not start. For surface-induced, melting we set $\varsigma = 0$ in the Ginzburg-Landau equation (8), since bulk perturbations are not required.

(b) To avoid surface-induced melting, we assume $\gamma_s = \gamma_m$. In this case, melting starts in the bulk after exceeding the temperature at which solid loses its stability. To model thermal fluctuations, one can introduce Langevin noise ς that satisfies the fluctuation-dissipation theorem[32,33]. This, however, requires a separate study and here we will use the simplest possible method to initiate bulk melting. Thus, we assume $\varsigma = 10^{-4}\, ps^{-1}$ if $\eta > 0.999999$ and $\varsigma = 0$ otherwise. Independent of the time step in the numerical integration, the piece-wise constant and homogeneous perturbation ς is introduced with a time step of $0.01ps$. Due to numerical errors in simulations, such a perturbation produces a random-like fluctuation of the order parameter as shown in Fig. 2. Without perturbation ς, the magnitude of numerical errors is several orders of magnitude smaller. Heating rate $Q = 84.15\, K/ps$ is considered for this regime.

The initial temperature is $T_0 = 293.15\, K$, the sample is initially stress free, and the initial $\eta = 0.999$ for all cases.

Material properties. The lattice heat capacities are described by

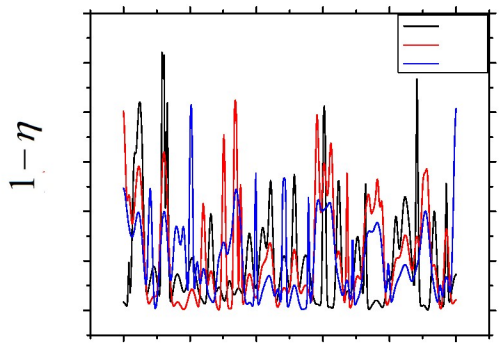

Fig. 2 Distribution of fluctuations of the order parameter introduced by perturbations for fluence of $13\, mJ/cm^2$.

the following equations[34]:

$$C_{ls} = (2434.86 + 1.457(T - 300.0)) \times 10^3\ J/(m^3K) \quad for \quad T < 900.0K;$$

$$C_{ls} = 3308.87 \times 10^3 J/(m^3K) \quad for \quad T > 900.0K;$$

$$C_{lm} = (2789.1 - 0.314(T - 933.0)) \times 10^3\ J/(m^3K). \tag{14}$$

The heat capacity of electron gas is $C_e = \bar{\gamma}T_e$, where $\bar{\gamma} = 91.2\, J/(m^3K^2)$ is the electron heat capacity constant[35]. For the electron-phonon coupling coefficient G, the theoretically calculated data is used[35]:

$$G = (3.663 - 1.218/(1 + (T_e \times 10^{-4}/0.221)^{2.294})) \times 10^{17}. \tag{15}$$

The electron thermal conductivity is approximated as $\kappa_e = \kappa_e^{eq} T_e/T$ to take into account the non-equilibrium effect[36,37]

$$\kappa_e^{eq} = \kappa_{em}^{eq} + \phi(\eta)(\kappa_{es}^{eq} - \kappa_{em}^{eq}), \tag{16}$$

where $\kappa_{es}^{eq} = 208\, W/(mK)$ for solid and $\kappa_{em}^{eq} = 102\, W/(mK)$ for melt[34]. The lattice thermal conductivity is $\kappa_l = 0.01\kappa_e$ (in Ref.[38]). The critical temperature for the loss of stability of melt is $T_c = 0.8\, T_{eq}$. Coefficients, constants, and properties used for the simulation are presented in Table 1[23].

3 Surface-induced melting and interface propagation

Some definitions. The melting of a 25-nm thin Al nanolayer irradiated by an ultrafast laser is simulated. Conditions and results are summarized in Table 2. In all simulations, the melting of a sample starts from both surfaces driven by the reduction in surface energy during melting. Melt nucleation away from the solid-melt interfaces was not observed. Fig. 3(a) shows the typical evolution of the order parameter η. The melting time, t_m, is defined as time from the moment of laser irradiation to the instant when two solid-melt interfaces collide and merge together; the position of an interface is defined by $\eta = 0.5$; and the point of meeting

Table 1 Properties of aluminum[23]

T_{eq} (K)	H (J/m^3)	K_m (GPa)	K_s (GPa)	μ (GPa)	ε_{0t}	α_m (K^{-1})	α_s (K^{-1})	γ_s (J/m^2)	γ_m (J/m^2)	β (N)	L (m^2/Ns)
933.67	933.57×10^6	41.3	71.1	27.3	0.06	4.268×10^{-5}	3.032×10^{-5}	1.050	0.921	3.21×10^{-10}	532

of interfaces (the melting center of the sample) is designated as x_{mc}. This definition is motivated by way of comparison with experiments, where melting time corresponds to the disappearance of x-ray peaks of solid phase. We define T_{ms} as the maximum superheating temperature of the solid during melting, which is reached at the melting center while $\eta > 0.5$. We designate time corresponding to T_{ms} as t_{ms}. As we will see t_{ms} is slightly smaller than t_m, because there is a temperature drop, down to the temperature T_{mf} at the end of melting (see Fig. 5). The surface melting time, t_{sm}, is defined as the time when the order parameter reaches 0.5 for the first time at the external surface and the surface melting temperature T_{sm} is defined as a temperature at the surface at t_{sm}. Heating rate is defined as $Q = \frac{T_{sm}-T_0}{t_{sm}}$ since for most cases temperature increases almost linearly before the initiation of melting.

Comparison with experiment in terms of melting time. For "slow" heating rate $Q = 0.015K/ps$, kinetic superheating is not observed and the melting temperature is as low as $T^{\epsilon}_{eq} = 898.1K$, i.e., significantly below T_{eq}. T^{ϵ}_{eq} is the equilibrium melting temperature under uniaxial strain conditions and corresponding biaxial stresses, which relax during melting[23], thus producing an additional thermodynamic driving force for melting and reducing melting temperature. This driving force exists for the high heating rate as well, but it is overpowered by kinetic factors and melting temperature significantly exceeds T_{eq}. The results for the slow heating are included in Table 2 in order to quantify superheating with respect to this temperature. As shown in Table 2, simulation results exhibit good agreement with experimental data in terms of melting time, except the strongest fluence case. The relative error between simulation result and the experimental measurement for the highest fluence is 29.5%; aside from this point, the relative error is 4.0% on average. With the current fully coupled lattice heat conduction and melting equations, the predictive capability of the simulation is significantly enhanced in comparison with the previous simulation[15], see Table 2 and Fig. 4(a).

Since part of the melting time is related to time of propagation of two interfaces through the sample until they meet, total melting time and, consequently, superheating increase with the sample thickness for this regime. For larger thicknesses, barrierless bulk melting can start in the remaining part of the sample and completes melting. In this case melting time and superheating are getting independent of the sample size.

While it may be surprising that the equilibrium melting occurs at constant temperature at the heating rate as high (from equilibrium perspective) as $0.015K/ps$, this can be supported by the balance of the supplied and absorbed energy rates. Thus, the averaged heating rate by a laser irradiation, $F_0/(wt_m^{exp}) = 4.0\times10^7 J/(m^3\, ns)$, is slightly lower than the averaged absorbed energy rate is $H/(t_m - t_{sm}) = 4.24\times10^7 J/(m^3\, ns)$,

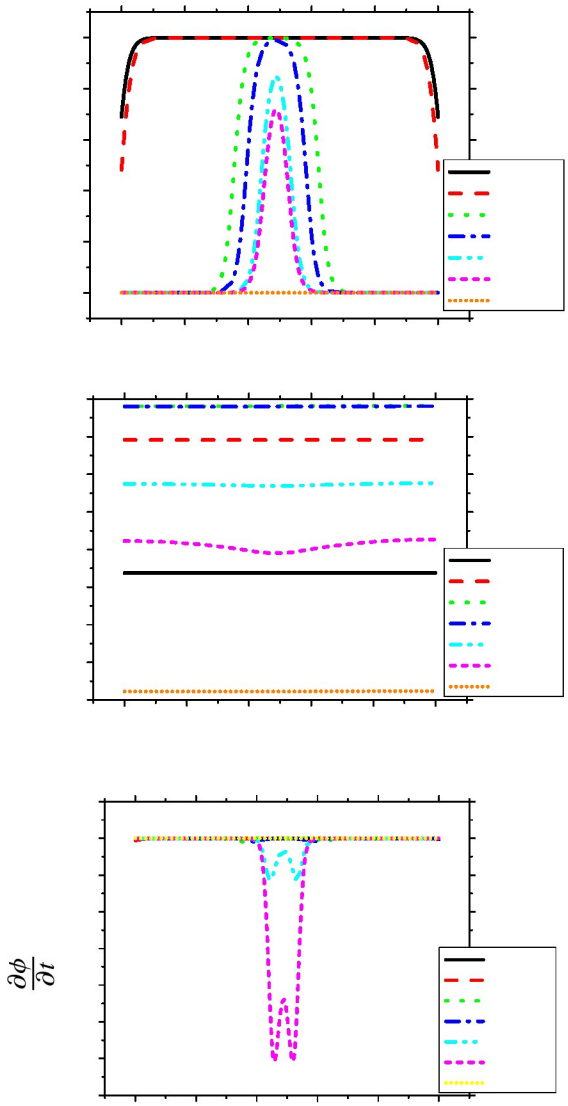

Fig. 3 Evolution of distributions of (a) the order parameter, (b) temperature, and (c) $\frac{\partial\phi}{\partial t}$ ($\phi = \eta^2(3-2\eta)$ is the interpolation function for variation of any material property between solid and melt) for $Q = 0.015\,K/ps$. When two interfaces collide, the magnitude of $\frac{\partial\phi}{\partial t}$ drastically grows and temperature reduces due to absorption of the heat of fusion.

Table 2 Summary of simulation conditions and results

Fluence ($F_0, mJ/cm^2$)	t_{sm} (ps)	t_{ms} (ps)	t_m^{exp} [a] (ps)	t_m (ps)	t_m [d] (ps)	Q (K/ps)	T_{sm} (K)	T_{ms} (K)	T_{mf} (K)	θ_c^ϵ	x_{mc} (nm)
10^{b}	41600	$6 \cdot 10^4$	10^5	63500		0.015	894.5	899.0	863.9	1.00	12.4
7	638	896	10^3	1013	789.8	0.99	921.9	971.8	784.8	1.08	12.35
8	216	321	350	344	296.8	3.20	983.4	1086.1	837.9	1.21	12.25
9	110	160	180	169	161.5	6.90	1052.4	1197.0	925.7	1.33	12.1
10	69	100	115	104.4	106.4	11.88	1112.5	1304.4	1004.3	1.45	11.95
11	38.5	57	60	58.5	63.6	24.55	1238.3	1532.5	1210.3	1.71	11.85
11[c]	37.5		60	58.0		25.26	1240.5	1538.6		1.71	11.85
13	15.4	21.2	20	25.7	27.7	83.04	1572.0	1963.8	1441.5	2.19	11.5
13[c]	15.4		20	25.9		84.15	1589.1	1971.2		2.19	11.55

[a] Pulse duration t_p in simulation is same as t_m^{exp} in the experiment.
[b] Imaginary slow heating case to evaluate equilibrium melting temperature modified by biaxial stress. t_m^{exp} for this case means the pulse duration in simulation.
[c] An elastodynamic formulation and waves are included.
[d] Simulated melting time without couplings [15].

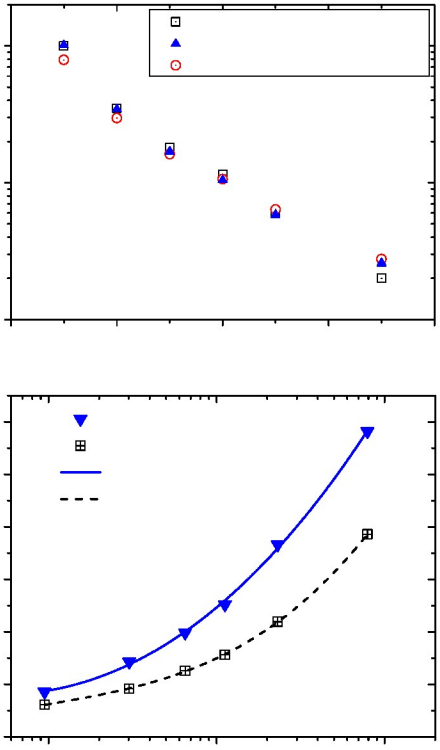

Fig. 4 (a) Melting time versus absorbed laser fluence obtained with the current model, model in Ref. [15], and in experiments [14], and (b) kinetic superheating and surface melting temperature versus the heating rate.

i.e., temperature increase is impossible.

Kinetic superheating. Since the solid-melt interface has finite velocity, the temperature of the solid at the center of a sample can reach much higher values than T_{sm} and T_{eq}^ϵ during fast heating before the interface arrives. Superheating factors are defined as $\theta_c^\epsilon = \frac{T_{ms}}{T_{eq}^\epsilon}$ and $\theta_c = \frac{T_{ms}}{T_{eq}}$. It is clear that $\theta_c/\theta_c^\epsilon = 0.96$. Evolution of temperature at point x_{mc} is presented in Fig. 5. The melting center x_{mc} shifts left as laser power becomes stronger (Table 2) because faster heating produces a larger temperature gradient and the right interface appears earlier and propagates faster than the left one. For slow heating with $Q = 0.015K/ps$, a plateau appears due to absorption of the latent heat, following initiation of melting around T_{eq}^ϵ. No superheating is observed; $T_{ms} \simeq T_{eq}^\epsilon$ and T_{sm} is slightly lower than T_{ms} because of surface premelting. With an increased heating rate, surface premelting and melting are delayed and T_{sm} increases. Temperature at x_{mc} grows during interface propagation and heat absorption, and transition to melting cannot be precisely detected by change of the temperature rate on the temperature evolution curves. Note that for all heating rates but $Q = 83.04K/ps$ melting time t_m is shorter than or similar to the laser pulse duration t_m^{exp}, i.e., laser heating occurs through the entire melting process. In contrast, for $Q = 83.04K/ps$ pulse duration is $20ps$ but melting time in the simulation is $25.7ps$. That is why the temperature decreases after $20ps$ due to absorption of heat of fusion (Fig. 5). This also partially explains the much larger melting time in simulations in comparison with the experiment.

Evolution of temperature distribution for different heating rates allows us to shed additional light on the melting process. Slow heating with $Q = 0.015K/ps$ does not cause a visible temperature gradient except at the very moment when melting ends, $t = 63.76\,ns$, and temperature at the melting center remains practically the same during melting (see Fig. 3(b) at time instants $60\,ns$ and $62\,ns$). Surprisingly, an increase in heating rates leads to the opposite effect of superheating: temperature reduction in some regions. Heating with $Q = 6.9\,K/ps$ results in a moderate temperature gradient before the initiation of melting (see plot for $100\,ps$ in Fig. 6(b)). The solid phase, which includes the melting center, heats up continuously after melting initiates at $t = 110\,ps$. On the other hand, in the surface melting zone and then at the moving solid-melt interface, temperature is lower than in the solid and even reduces in time. This

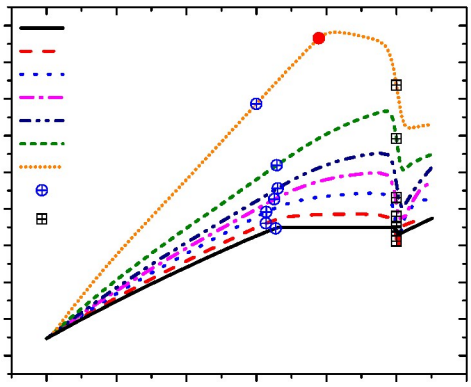

Fig. 5 Evolution of temperature at the melting center for different heating rates. Red circle represents the end moment of laser pulse for $Q = 83.04\,K/ps$.

happens due to absorbed heat of fusion. The maximum temperature difference between the interface and solid exceeds $250\,K$. Fig. 7 helps to understand contribution of different terms in the temperature evolution equation, Eq.(10), to the evolution of the temperature profile at the finite-width interface. The largest contribution to the temperature reduction is because of the term $-\left[3p_e\Delta\alpha - \frac{H}{T_{eq}}\right]T\frac{\partial\phi}{\partial\eta}\frac{\partial\eta}{\partial t}$ (note that $\frac{\partial\phi}{\partial\eta}\frac{\partial\eta}{\partial t} < 0$) due to heat of fusion and change in the thermal expansion coefficient. The second, much smaller, negative contribution is caused by thermoelastic coupling $-3T\left(\alpha_m + \Delta\alpha\phi\right)\frac{\partial p_e}{\partial t}$, because $\frac{\partial p_e}{\partial t} > 0$ due to the relaxation of elastic compressive pressure during melting. There is an even smaller positive contribution to the temperature increase due to the dissipation rate of melting, $\left(\frac{\partial\eta}{\partial t}\right)^2/L$. Similar patterns are common for $Q > 0.99\,K/ps$.

Collision of two interfaces. One more surprise consists of a rapid temperature drop at the end of melting, i.e., just after $t/t_{ms} = 1.0$ (Figs. 3(b), 5, and 6(b)). For the smallest heating rate in Fig. 3(b), there is no temperature decrease at the moving interfaces and temperature is practically homogeneous except in the final moment of melting. However, immediately after $t/t_{ms} = 1.0$, temperature almost homogeneously drops down to $T_{mf} = 863.9K$, i.e., significantly below T_{eq}. The only reason for this is the overlap of interfaces, which continues until η reaches zero everywhere. During this time the magnitude of the rate $\frac{\partial\phi}{\partial t}$ (Fig. 3(c)) and, consequently, the heat absorption rate $H\frac{T}{T_{eq}}\frac{\partial\phi}{\partial t}$ (see Eq.(10)) increases drastically, which causes the temperature drop. This means that the overlapping interfaces attract each other and accelerate melting; the degree of acceleration of melting in fact characterizes attraction of interfaces. Homogeneity of the temperature even during the drop is caused by relatively slow heating and melting. A similar phenomenon occurs, and is even more pronounced, for high heating rates (Fig. 6). It superposes on the temperature drop that takes place at the moving interfaces due to absorption of the heat of fusion. In Fig. 6(c), the maximum magnitude of $\frac{\partial\phi}{\partial t}$ at the moving interface grows slightly only due to an increase in temperature before interfaces start overlap-

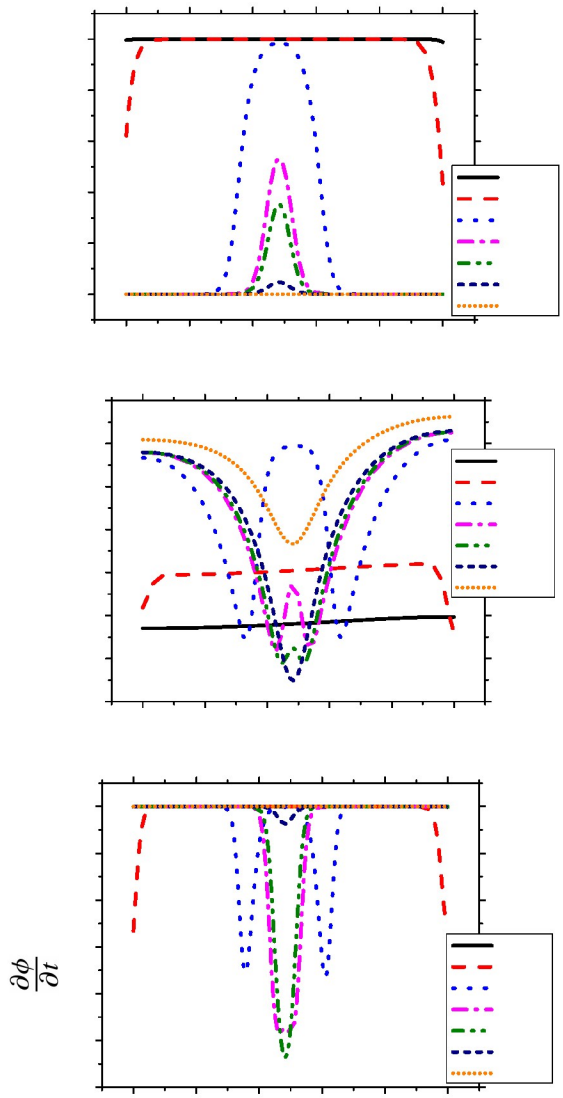

Fig. 6 Evolution of the distributions of (a) the order parameter, (b) temperature, and (c) $\frac{\partial\phi}{\partial t}$ for $Q = 6.9\,K/ps$.

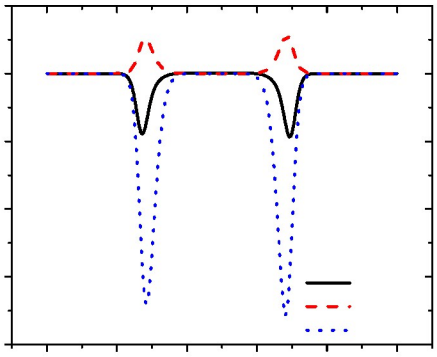

Fig. 7 Contribution of three source terms in the temperature evolution equation (10) at $150\,ps$ for $Q = 6.9\,K/ps$: the third term, $-3T(\alpha_m + \Delta\alpha\phi)\frac{\partial p_e}{\partial t}$ due to thermoelastic coupling, the fourth term, $\left(\frac{\partial \eta}{\partial t}\right)^2/L$ due to the dissipation rate of melting, and the fifth term $-\left[3p_e\Delta\alpha - \frac{H}{T_{eq}}\right]T\frac{\partial \phi}{\partial \eta}\frac{\partial \eta}{\partial t}$ due to heat of fusion and change in thermal expansion coefficient.

ping. After overlapping, $\frac{\partial \phi}{\partial t}$ increase significantly and causes localized temperature drop near the melting center. Localization is due to the high heating and melting rate, as well as relatively slow heat transfer. Since the same (or similar) absorption of heat causes temperature reduction in a smaller region than for $Q = 0.015K/ps$, the magnitude of temperature drop is significantly larger. Integration of $\frac{\partial \phi}{\partial t}$ over volume gives an overall rate of the heat absorption in the sample and shows a sharp peak just after reaching t_{ms} and T_{ms} (Fig. 8).

Analytical approximation of function T_{ms} and T_{sm} vs. $log\,Q$ plotted in Fig. 4(b) are: $T_{ms} = 976.49 + 111.11\,log\,Q + 192.65(log\,Q)^2 + 12.43(log\,Q)^3$ ($R^2 = 0.998$) and $T_{sm} = 924.24 + 112.40 log\,Q - 1.94(log\,Q)^2 + 64.57(log\,Q)^3$ ($R^2 = 0.9998$).

Effect of elastic wave. For very fast heating at the picosecond scale, when melting time reduces and becomes comparable with acoustic time, dynamic treatment is required. Plots of evolution of stress σ_{11} and elastic mean stress p_e before melting are presented in Fig. 9. Since σ_{11} does not receive contributions from the interface stresses, $\sigma_{11} = \sigma^e_{11}$; then $\sigma^e_{22} = \sigma^e_{33} = (3p_e - \sigma_{11})/2$ can be evaluated based on plots in Fig. 9. Due to a temperature increase under constraint of uniaxial strain conditions, compressive stresses $\sigma_{22} = \sigma_{33}$ grow within the layer. They cause growth of the compressive stress σ_{11}, with the maximum at the center and zero values at the surfaces, due to boundary conditions. A standing wave with nodes at the surfaces and wave length $\lambda = 2w$ is formed, in which stress σ_{11} oscillates around the zero value (which is the static solution) with the magnitude of $1.25GPa$ (reaching maximum tensile stress at 6 ps) and stresses $\sigma_{22} = \sigma_{33}$ oscillate around growing compressive stress. When melting occurs at the surfaces, compressive stresses $\sigma_{22} = \sigma_{33}$ and stress σ_{11} relax in melt down to zero. During melting, solid-melt interfaces become new nodal points so that pressure oscillates between two interfaces within the solid with reducing magnitude, which is relatively small compared to the pressure for elastostatic

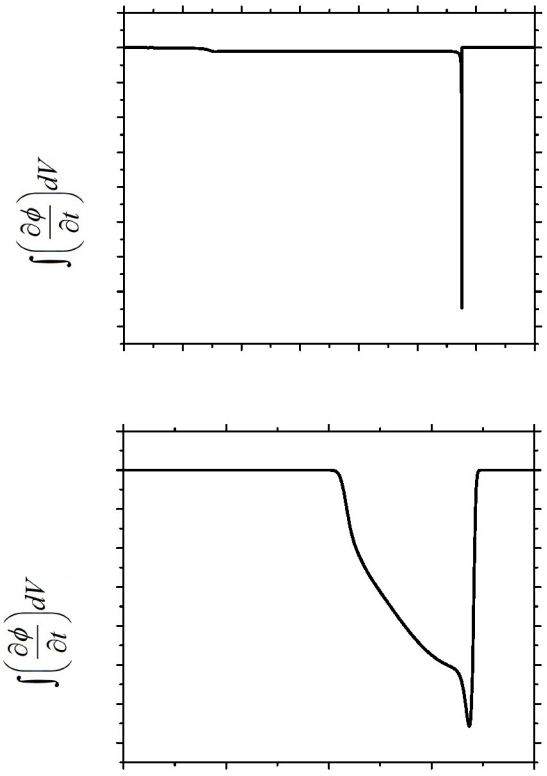

Fig. 8 Evolution of the volume integral of $\frac{\partial \phi}{\partial t}$ for (a) $Q = 0.015K/ps$ and (b) $Q = 6.9K/ps$

.

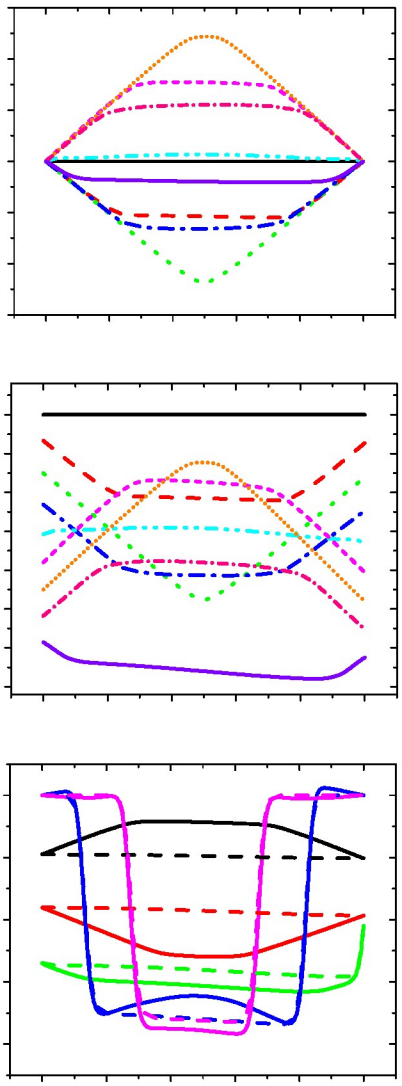

Fig. 9 Evolution of (a) σ_{11}, (b) p_e distributions before melting starts, and (c) comparison of evolution of elastic mean stress p_e distribution for simulation in elastostatic (solid line) and elastodynamic (dashed line) formulations for $Q = 84.15\ K/ps$.

formulation (Fig. 9(c)). As shown in Table 2, elastic waves do not remarkably affect characteristic melting times and temperatures. The reasons for this small effect follow from Fig. 9(c), where elastic pressure distribution for elastostatic and elastodynamic formulations are compared. Nodal points at both surfaces mean that the surface is not affected by elastic waves and the elastic pressure at surfaces is the same in both formulations. That is why conditions for surface-induced melt nucleation and T_{sm} in Table 2, which depend on pressure distribution near external surfaces, are very close. Pressure distribution within interfaces is very similar in both formulations and, consequently, does not affect interface velocity.

4 Bulk melting

Problem formulation based on initiation of surface-induced melting and without fluctuations in bulk led to good correspondence between calculated and experimental melting times for $Q \leq 25.26\ K/ps$ (see Table 2). For the fastest heating rate $Q \geq 83\ K/ps$, calculated melting time is 29.5% larger than the experimental one and maximum superheating temperature is well above the temperature at which the solid loses its thermodynamic stability (in the current model, at $1.2T_{eq} = 1120K$). This means that, in addition to surface melting followed by propagation of interfaces toward the sample center, barrierless melting in the bulk may occur, which will accelerate melting and reduce maximum superheating. For a thick enough sample, the time for bulk melting may be much smaller than the time before two interfaces meet; that is why surface melting is not important. Surface melting can also be avoided if one reduces the difference between surface energies of a solid and melt, $\gamma_s - \gamma_m$, e.g., by placing at the surface crystal faces which do not undergo surface melting, changing surrounding, or producing proper surface treatment. To study bulk melting, we set $\gamma_s = \gamma_m$ in the boundary condition (Eq.(13)) and specified the perturbation term ς in Ginzburg-Landau equation (Eq.(8)) to initiate the bulk melting.

Results for elastodynamic and elastostatic problem formulations are presented in Fig. 10 and compared with previous elastodynamic simulations for surface-induced melting. Melting starts quasi-homogeneously within the entire sample, while melting in the right side is slightly more advanced because of the higher temperature. Since the tracking order parameter at the melting center is meaningless for this case, $\bar{\phi} = \frac{1}{w}\int \phi dx$ is calculated in order to compare melting time with surface-induced melting. t_m **is defined as the time to reach** $\bar{\phi} = 0.1$. In elastostatic formulation, melting near the right surface progresses and completes significantly faster than near the left surface. For elastodynamic formulation, the standing p_e wave in Fig. 9(b) has a maximum in the central region of the sample. Since the temperature of the sample is above the solid instability temperature, $1.2T_{eq}$, pressure oscillation promotes melting by lowering the equilibrium melting temperature and solid instability temperature in its tensile peak without essential suppressing melting in its compression stage. Distribution of the order parameter is less heterogeneous than in elastostatic formulation. While bulk melting starts later and at a higher temperature than the surface-induced melting, it completes faster. **Thus,** t_m **for bulk melting is** $22.7ps$ **(**$6.3fs$ **standard deviation) and** $21.9ps$ **(**$176.5fs$ **standard deviation) for elastostatic and elastodynamic formulation, respectively. Here, the melting time,** t_m**, is calculated as an average over 10 simulation cases due to the stochastic nature of random fluctuation.** It is significantly closer to experimentally measured time, $20ps$, than $25.7ps$ for surface-induced melting (Table 2). **Melting time for bulk melting is independent of the sample thickness in a range, when bulk melting is possible. More precise study in which thermal fluctuations are included that satisfy the fluctuation-dissipation theorem[32,33] will be pursued in the future.**

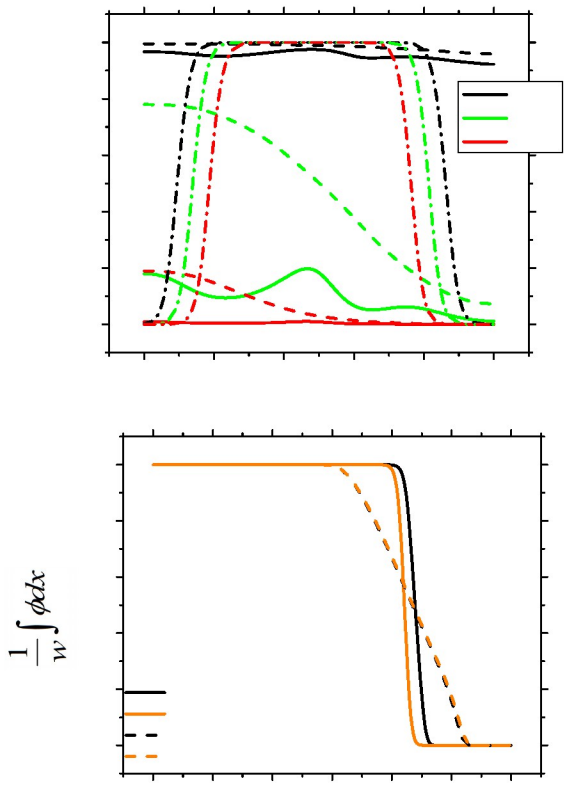

Fig. 10 Time evolution of distribution of (a) the order parameter η and (b) the $\frac{1}{w}\int \phi dx$ for the fluence $13\,mJ/cm^2$. In figure (a), solid and dashed lines represent bulk melting in elastodynamic and elastostatic formulations and dash-dot line is elastodynamic simulation of the surface-induced melting. **The representative case out of 10 computations for bulk melting is presented.**

5 Conclusions

Main results. An advanced thermodynamically consistent model for kinetic superheating and melting of an Al nanolayer irradiated by a picosecond laser is formulated. It includes the coupled system of phase field equations for melting, the two-temperature model for electron and lattice heat conduction, and the equations of elastodynamics that allow for interface stresses. The Ginzburg-Landau equation for melting is fully coupled with elastodynamic and lattice thermal conduction. The lattice heat conduction equation includes electron-phonon coupling, heat of fusion, thermoelastic effects, and the dissipation rate due to melting. Reduction in surface energy during the melting is included in the boundary conditions for the order parameter. This system of equations was solved using finite element method and code COMSOL Multiphysics. Such a sophisticated physical formulation allowed us both to describe some nontrivial experimental results and reveal new phenomena. Two main regimes were considered. In the first one, barrierless nucleation of surface premelting and melting occurs followed by the propagation of two solid-melt interfaces toward each other and their collision. For the slow heating rate $Q = 0.015\,K/ps$ melting occurs at the equilibrium melting temperature under uniaxial strain conditions $T^{\epsilon}_{eq} = 898.1K$ (i.e., below $T_{eq} = 933.67\,K$) and corresponding biaxial stress, which relax during melting. For a high heating rate $Q = 0.99 - 84\,K/ps$, significant overheating above T_{eq} is observed before complete melting. Surprisingly, an increase in the heating rate leads to a temperature reduction at the moving interfaces due to fast heat of fusion absorption. A significant, rapid temperature drop (even below melting temperature) at the very end of melting is revealed, which is caused by the collision of two interfaces and accelerated melting. For $Q = 25 - 84\,K/ps$, standing elastic stress waves are observed in the solid with nodal points at the moving solid-melt interfaces, which however, do not have a profound effect on melting time and temperatures. Simulation results are in good correspondence with known experiments[14] in terms of time for complete melting, excluding the highest heating rate $Q = 84\,K/ps$. For the second regime and the highest heating rate of $84\,K/ps$, the surface melting was suppressed but bulk thermal fluctuations have been mimicked in a simple way. In this case, barrierless bulk melting occurs in the entire sample. Elastodynamic effects are more important than in the first regime and much better correspondence with experimental melting time is obtained.

Future directions. **The same approach can be applied to other metals by simply changing material parameters.** Similar approaches are applicable to study various phase transformations (martensitic, reconstructive, amorphization, etc.) in different materials (metals, ceramics, and nanocomposites) and nanostructures (single and multilayers, nanoparticles, nanowires, and core-shell structures) under high heating rates. In particular, instead of (or in addition to) the Ginzburg-Landau equation for melting, one can utilize equations for martensitic transformations, twinning, dislocations, and their interaction[28,39–41]. Also, surface melting (phase transformations) can be described more precisely if one explicitly introduces the finite width of the external surface[42,43]. This can also be done by considering

nucleation of melt within an interface between two phases[44].

6 Acknowledgments

Support from ONR (USA), Agency for Defense Development, Seyeon E&S corporation, and Gyeongsang National University (all South Korea) is gratefully acknowledged.

References

1 W. Nichols, G. Malyavanatham, D. Henneke, D. O'Brien, M. Becker and J. Keto, *J. Nanopart. Res.*, 2002, **4**, 423–432.
2 Z. Yan, Q. Zhao and D. B. Chrisey, *Mater. Chem. Phys.*, 2011, **130**, 403 – 408.
3 P. Serra, M. Duocastella, J. Fernández-Pradas and J. Morenza, *Appl. Surf. Sci.*, 2009, **255**, 5342 – 5345.
4 X. Chen, Y. Chen, J. Dai, M. Yan, D. Zhao, Q. Li and M. Qiu, *Nanoscale*, 2014, **6**, 1756–1762.
5 P. Kazansky, M. Beresna, Y. Shimotsuma, K. Hirao and Y. P. Svirko, LEOS Annual Meeting Conference Proceedings, 2009. LEOS '09. IEEE, 2009, pp. 330–331.
6 V. I. Levitas, *Philos. Trans. Roy. Soc. A*, 2013, **371**, 20120215.
7 Q. Mei and K. Lu, *Prog. Mater. Sci.*, 2007, **52**, 1175 – 1262.
8 J. Cheng, C. Liu, S. Shang, D. Liu, W. Perrie, G. Dearden and K. Watkins, *Opt. Laser Technol.*, 2013, **46**, 88–102.
9 B. Rethfeld, K. Sokolowski-Tinten, D. von der Linde and S. I. Anisimov, *Phys. Rev. B*, 2002, **65**, 092103.
10 S. Luo and T. J. Ahrens, *Appl. Phys. Lett.*, 2003, **82**, 1836–1838.
11 S. Luo, T. J. Ahrens, T. Çağın, A. Strachan, W. A. Goddard III and D. C. Swift, *Phys. Rev. B*, 2003, **68**, 134206.
12 J. Wei, Z. Sun, F. Zhang, W. Xu, Y. Wang, F. Zhou and F. Gan, *Chem. Phys. Lett.*, 2004, **392**, 415–418.
13 B. J. Siwick, J. R. Dwyer, R. E. Jordan and R. J. Dwayne Miller, *Science*, 2003, **302**, 1382–1385.
14 S. Williamson, G. Mourou and J. C. M. Li, *Phys. Rev. Lett.*, 1984, **52**, 2364–2367.
15 Y. S. Hwang and V. I. Levitas, *Appl. Phys. Lett.*, 2013, **103**, 263107.
16 M. V. Shugaev and N. M. Bulgakova, *Appl. Phys. A*, 2010, **101**, 103–109.
17 A. Amini, C. Cheng, M. Naebe, J. S. Church, N. Hameed, A. Asgari and F. Will, *Nanoscale*, 2013, **5**, 6479–6484.
18 Y. Meshcheryakov, M. Shugaev, T. Mattle, T. Lippert and N. Bulgakova, *Appl. Phys. A*, 2013, **113**, 521–529.
19 Y. Zhang and J. K. Chen, *J. Appl. Phys.*, 2008, **104**, 054910.
20 K. Baheti, J. Huang, J. Chen and Y. Zhang, *Int. J. Therm. Sci.*, 2011, **50**, 25 – 35.
21 D. Sowdari and P. Majumdar, *Opt. Laser Technol.*, 2010, **42**, 855 – 865.
22 H. J. Fecht and W. L. Johnson, *Nature*, 1988, **334**, 50–51.
23 Y. S. Hwang and V. I. Levitas, *Appl. Phys. Lett.*, 2014, **104**, 263106.
24 V. I. Levitas and K. Samani, *Phys. Rev. B*, 2011, **84**, 140103(R).
25 V. I. Levitas and K. Samani, *Nat. Commun.*, 2011, **2**, 284.
26 V. I. Levitas and M. Javanbakht, *Phys. Rev. Lett.*, 2010, **105**, 165701.
27 V. I. Levitas, *Acta Mater.*, 2013, **61**, 4305 – 4319.
28 V. I. Levitas, *J. Mech. Phys. Solids*, 2014, **70**, 154 – 189.
29 B. Rethfeld, A. Kaiser, M. Vicanek and G. Simon, *Phys. Rev. B*, 2002, **65**, 214303.
30 N. Provatas and K. Elder, *Phase-Field Methods in Materials Science and Engineering*, WILEY-VCH, Weinheim, 1st edn., 2010.
31 *COMSOL Multiphysics Reference Manual*, COMSOL, 2014.
32 R. Kubo, *Rep. Prog. Phys.*, 1966, **29**, 255.
33 A. Karma and W.-J. Rappel, *Phys. Rev. E*, 1999, **60**, 3614–3625.
34 *Aluminum: Properties and Physical Metallurgy*, American Society for Metals, 10th edn., 2005.
35 Z. Lin, L. V. Zhigilei and V. Celli, *Phys. Rev. B*, 2008, **77**, 075133.
36 A. N. Smith, J. L. Hostetler and P. M. Norris, *Numer. Heat Transfer, Part A*, 1999, **35**, 859–873.
37 P. J. Antaki, *Int. J. Heat Mass Tran.*, 2002, **45**, 4063–4067.
38 B. Giordanengo, N. Benazzi, J. Vinckel, J. G. Gasser and L. Roubi, *J. of Non-Cryst. Solids*, 1999, **250**, 377–383.
39 V. I. Levitas and D.-W. Lee, *Phys. Rev. Lett.*, 2007, **99**, 245701.
40 V. I. Levitas and M. Javanbakht, *J. Mech. Phys. Solids*, 2015, **82**, 287–319.
41 V. I. Levitas and M. Javanbakht, *Nanoscale*, 2014, **6**, 162–166.
42 V. I. Levitas and M. Javanbakht, *Phys. Rev. Lett.*, 2011, **107**, 175701.
43 V. I. Levitas and K. Samani, *Phys. Rev. B*, 2014, **89**, 075427.
44 K. Momeni, V. I. Levitas and J. A. Warren, *Nano Lett.*, 2015, **15**, 2298–2303.